Research article

Core-shell Ni/SiO$_2$@ZrO$_2$ catalyst for highly selective CO$_2$ conversion accompanied by enhancing reaction stability

Sha Cui [a,c,d,*], Zhe Wang [a], Honggang Zhao [a], Houxiang Sun [b], Qinhong Wei [a], Luhui Wang [a]

[a] *School of Petrochemical Engineering & Environment, Zhejiang Ocean University, Zhoushan, 316022, China*
[b] *School of Biology and Chemical Engineering, Panzhihua University, Panzhihua, 617000, China*
[c] *Zhejiang Provincial Key Laboratory of Petrochemical Pollution Control, Zhejiang Ocean University, Zhoushan, 316022, China*
[d] *National-Local Joint Engineering Laboratory of Harbor Oil & Gas Storage and Transportation Technology, Zhejiang Ocean University, Zhoushan, 316022, Zhejiang, China*

A R T I C L E   I N F O

A B S T R A C T

CO$_2$ RWGS reaction was considered to be a promising process for carbon dioxide conversion, however it retained a big challenge owing to methanation and metal sintering. Therefore, it was desperately needed to devise highly selective and stable catalyst. Herein, core-shell Ni/SiO$_2$@ZrO$_2$ catalyst was successfully prepared via a combination of the wet impregnation and in-situ hydrothermal synthesis method, with ZrO$_2$ as the coating shell. The optimized Ni/SiO$_2$@4ZrO$_2$ catalyst possessed enhanced metal-support interaction and rich oxygen vacancies as well as abundant medium-strength CO$_2$ adsorption sites. As a result, under the GHSV of 120000 mL/g·h and 150000 mL/g·h, Ni/SiO$_2$@4ZrO$_2$ displayed a considerable hydrogenation activity and significantly higher selectivity to CO, compared with the Ni/SiO$_2$ catalyst as a reference. During stability tests, Ni/SiO$_2$@4ZrO$_2$ also showed a superior catalytic stability with a steady 100 % CO selectivity, carried out at 600 °C for 72 h. This work provided a novel strategy of designing a core-shell catalyst for CO$_2$ RWGS reaction, and was expected to be put into use in other multiphase reaction process.

1. Introduction

As global warming and climate change became increasingly problematic, the reduction strategies of greenhouse gas emission had attracted wide attention in terms of basic research and industrial applications. Carbon dioxide was the major contributor to the greenhouse effect and greatly increased due to the excessive consumption of coal, oil and natural gas [1]. Therefore, it was an urgent and common goal pursued by the international community to reduce carbon dioxide emissions [2,3]. In this case, applying CO$_2$ as an alternative carbon source and converting it into high value-added chemicals and fuels satisfied the need to achieve large-scale carbon fixation, carbon emission reduction and carbon cycling. The use of blue and green hydrogen (H$_2$) from renewable sources to react with CO$_2$ to produce CO (RWGS, Eq. (1)) was a sustainable development direction that effectively utilized this abundant and relatively cheap carbon resource [4]. And the produced CO or syngas (CO + H$_2$) was a key chemical platform molecule for conversion into other high value-added chemicals, such as methanol, high-carbon alcohols and other liquid fuels [5,6]. Moreover, most syngas conversion

---

* Corresponding author. School of Petrochemical Engineering & Environment, Zhejiang Ocean University, Zhoushan, 316022, China.
E-mail address: cuisha2019@zjou.edu.cn (S. Cui).

was relatively mature in commercial technology and could play a huge use of CO [7]. However, due to the thermodynamic stability of CO_2, the numerous parallel reactions in the CO_2 hydrogenation process and uncontrollable C-C coupling steps, it was difficult to balance the activity and selectivity [8]. Therefore, it was the core issue to achieve efficient and selective conversion of CO_2 to CO for RWGS reaction, and the key was the development of catalyst.

$$CO_2 + H_2 \rightarrow CO + H_2O, \Delta H_{298K}^0 = +41.5 kJ/mol \tag{1}$$

$$CO_2 + 4H_2 \rightarrow CH_4 + 2H_2O, \Delta H_{298K}^0 = -165 kJ/mol \tag{2}$$

$$CO + 3H_2 \rightarrow CH_4 + H_2O, \Delta H_{298K}^0 = -206.1 kJ/mol \tag{3}$$

Up to now, numerous catalysts had been studied for RWGS reaction to tend to produce CO, including noble metal as Pt-, Au- and Ir-based catalysts [9–12], and transition metal as Ni- and Cu-based catalysts [13–15]. The endothermic RWGS reaction required a higher reaction temperature, which often gave rise to agglomerating and sintering of metal catalysts, especially Cu-based catalysts. Considering economic benefits and natural reserves, noble metals could not be widely exploited. Ni-based catalyst had been widely used in RWGS reaction because of its economic viability and relatively high hydrogenation ability. However, the process of hydrogenation reduction of carbon dioxide to carbon monoxide was often accompanied by severe methanation reaction (Eq. (2) and Eq. (3)), and its competitive effect had a great influence on the selectivity of RWGS products. In fact, methane was the world's second largest greenhouse gas after carbon dioxide [16], and CH_4 was a very stable molecule, and its further conversion was much more difficult than CO [17]. In order to improve the CO selectivity and stability, many researchers had explored a variety of modification strategies and methods for Ni-based catalysts. Considering the effective promotion to CO formation, reducing the size of nickel nanoparticles was frequently used. Wu et al. [18] employed Ni/SiO_2 with 0.5 wt% and 10 wt% Ni loading for catalytic CO_2 hydrogenation reaction. The 0.5 wt% Ni/SiO_2 catalyst with small Ni particle size showed a comparatively higher CO selectivity, however the 10 wt% Ni/SiO_2 catalyst with large Ni grain size and a low dispersion was inclined to favor CH_4 formation. Goncalves et al. [19] prepared the Ni/SiO_2 catalyst via a magnetron sputtering deposition method, and the catalyst exhibited small grain size, thus a high CO selectivity. Ni-based bimetallic catalysts have been widely studied for enhancing RWGS reaction performance. Zhu and coworkers [20] proposed the deposition of Ag on the surface of Ni-based catalyst, where Ag improved the properties of Ni through geometric and electronic effects which facilitated CO desorption and blocked undesirable methanation reaction. Yang et al. [21] found that $Ni-FeO_X/CeO_2-Al_2O_3$ exhibited the superior catalyst performance in the reaction of RWGS than $Ni/CeO_2-Al_2O_3$ as a reference catalyst, not only in terms of activity, but also in terms of stability and selectivity towards CO, on account of the strong interaction between FeO_X and Ni particles. Beyond that, regulating the metal-support interaction (MSI) was an important strategy to promote the catalytic activity and improve the stability of supported metal nanoparticles. Rutherford et al. [22] compared Ni-based catalysts supported on Al_2O_3, ZnO, Fe_2O_3 and Co_3O_4 for RWGS reaction, and discovered that Ni/Co_3O_4 displayed upper CO selectivity which was realized by the metal-support interaction (MSI) between Ni and Co_3O_4 that suppressed CH_4 formation. Wang et al. [23] found that the strong metal-support interactions between Ni and ZnO showed a remarkable positive effect on the CO selectivity, the light-degree MSI state however facilitated promotion of the CH_4 selectivity and stability of methanation.

As was well-known that the support acted a pivotal role in supported Ni-based catalysts, reflected in facilitating Ni dispersion, modifying Ni electronic properties, introducing oxygen vacancy and mobility [24–26]. Various supports have been investigated for Ni-based catalysts, such as SiO_2 [27,28], Al_2O_3 [29,30], CeO_2 [24,31], TiO_2 [32,33], ZnO [34] and ZrO_2 [35–37]. SiO_2 was widely used as a carrier for various heterogeneous catalysts because of its rich content, low cost and high specific surface area. Traditional silica had long been considered as an inert carrier for dispersing active metals or for exploring reaction mechanisms of heterogeneous catalysis [38]. ZrO_2 was a P-type semiconductor and showed superior speciality as a reducible support or promoter for CO_2 hydrogenation reaction, could provide abundant oxygen vacancies that facilitated the activation and reduction of CO_2 [39]. Moreover, ZrO_2 had hydrophilic characteristics that was conducive to the desorption of produced water [40,41], and this would definitely facilitate the RWGS reaction.

After considering the strategies above, in our work, Ni/SiO_2 was first prepared by wet impregnating method. Then the as-synthesized Ni/SiO_2 was used as the core material for coating with ZrO_2 shell via in-situ hydrothermal process. And the core-shell $Ni/SiO_2@ZrO_2$ materials composed of Ni/SiO_2 core and ZrO_2 shell was prepared. The permeable porous shell of the core-shell catalyst protected metal particles from agglomeration and sintering [42,43], or provide a controlled nanopore environment facilitating the hydrogenation of CO_2 to CO [44]. The formed $Ni/SiO_2@ZrO_2$ catalyst was tested for RWGS reaction at 400–600 °C, and Ni/SiO_2 was used as a comparison. The CO_2 conversion and CO selectivity was tested in order to evaluate the activity and stability of catalyst for RWGS reaction.

2. Experimental

2.1. Catalyst preparation

The core-shell $Ni/SiO_2@ZrO_2$ catalyst was prepared via a combination of the wet impregnation and in-situ hydrothermal synthesis method. First, Ni/SiO_2 was prepared by a wet saturated volume impregnation method. In detail, 0.55 g of nickel nitrate (Ni $(NO_3)_2 \cdot 6H_2O$) was added to about 2 mL of deionized water (determined by the water absorption of SiO_2). After forming a uniform solution, 1 g of SiO_2 support was added to above solution and left for 12 h. Afterwards the sample was dried at 100 °C overnight,

calcined at 600 °C for 3 h and reduced in hydrogen in-situ at 600 °C before reaction. The nickel weight percentage was calculated 10 wt %. Then, the above calcined Ni/SiO_2 powder was dispersed in 50 mL of ethanol in vibration, followed by adding 2 mL and 4 mL $ZrOCl_2$ solution (Zr molar concentration of 1 mol/L). 28 wt% ammonia solution was then added dropwise to the above solution for regulating pH ~ 9, then further stirred at room temperature for 2 h. The resultant suspension was further transferred into autoclaves for hydrothermal reaction at 150 °C for 12 h. Subsequently, the initially obtained $Ni/SiO_2@ZrO_2$ was collected by centrifugation and washing repeatedly. The collected sample was dried, calcined and reduced under the same conditions. The catalysts were denoted to $Ni/SiO_2@2ZrO_2$ and $Ni/SiO_2@4ZrO_2$, respectively.

2.2. Catalyst characterization

X-Ray Diffraction (XRD) was used for the crystalline structures of Ni/SiO_2, $Ni/SiO_2@2ZrO_2$ and $Ni/SiO_2@4ZrO_2$ catalysts and the XRD patterns were obtained on a Rigaku SmartLab SE X-ray Diffractometer. The samples were measured from 10° to 80° at a scanning rate of 2°/min.

The elemental composition of catalysts was determined by ICP-OES and measured by Agilent 720-ES.

H_2-TPR and CO_2-TPD measurements were carried out by a PCA-1200 analyzer. The H_2-TPR experiment was carried out to illustrate the reducibility of nickel catalysts and the CO_2-TPD test was performed to obtain the information of the type and number of CO_2 adsorption active sites. Prior to the experiments, 100 mg of the catalyst precursor was pretreated in Ar gas at 200 °C to remove the impurity adsorbed on the surface. Then for the H_2-TPR, the calcined catalysts of Ni/SiO_2, $Ni/SiO_2@2ZrO_2$ and $Ni/SiO_2@4ZrO_2$ were reduced in H_2/Ar (10 % H_2) flow of 40 mL/min from 20 °C to 890 °C at a heating rate of 5 °C/min and so the H_2-TPR curve was recorded. And for the CO_2-TPD, the pretreated catalyst precursor was firstly reduced by H_2 at 600 °C for 2 h and subsequently cooled down to 100 °C. Then after an adsorption of CO_2 gas for 1 h, the sample was purged with a Ar flow (20 mL/min) for 10 min. Afterwards, CO_2 desorption was proceeded from 100 °C to 700 °C in Ar flow at a heating rate of 5 °C/min and the desorbed CO_2 was detected by TCD.

X-ray photoelectron spectroscopy (XPS) was used to obtain information about the composition, chemical state and molecular structure of the elements on the surface of the sample. And the XPS spectra of the freshly reduced Ni/SiO_2, $Ni/SiO_2@2ZrO_2$ and $Ni/SiO_2@4ZrO_2$ were acquired with an American Thermo Scientific K-Alpha spectrometer equipped with a Al-Ka source and an optimum analytical vacuum of 5.0×10^{-7} mbar. The binding energies (BE) was obtained with C1s = 284.80 eV as the standard.

Transmission electron microscopy (TEM) was measured to observe the morphology of the sample, the dispersion of the metal active phase and the particle size distribution. And the TEM photograph was determined with a FEI Tecnai G2 F20 electronic microscope. The interplanar distance was analyzed by Gatan DigitalMicrograph software and particle size distribution was calculated by Nano Measure 1.2 software.

2.3. Catalyst tests

The CO_2 hydrogenation activity evaluation was executed in a fixed bed reactor equipped with a 8 mm quartz tube. A certain amount of catalyst was evenly mixed with quartz sand and then loaded in the middle of the quartz tube. The catalyst filling amount was 40 mg and 50 mg, and the corresponding weight-hour space speed was 150000 mL/g·h and 120000 mL/g·h. Before the reaction, the catalyst precursor was reduced in-situ with 20 % H_2/N_2 atmosphere from room temperature to 600 °C and then maintained for 1 h. Subsequently, the reactor was cooled to 400 °C and then introduced of reactive gas composed of 40 mL/min CO_2, 40 mL/min H_2 and 20 mL/min N_2. The reaction was carried out under atmospheric pressure. The reaction temperature was set to increase from 400 °C to 600 °C, and then drop to 400 °C with the temperature interval of 50 °C. Each reaction temperature was kept for 1 h, and chromatographic analysis was performed four times. The reaction data were calculated by averaging the four test data. The conversion (X) and reaction rates (R) of CO_2, as well as CO selectivity (Y_{CO}) were calculated according to the following formula:

$$X_{CO_2} = \frac{[CO_2]_{in} - [CO_2]_{out}}{[CO_2]_{in}} \times 100\%$$

$$R = \frac{[CO_2]_{in} * X_{CO_2}}{m * w_{Ni}} \times 100\%$$

$$Y_{CO} = \frac{[CO]_{out}}{[CO]_{out} + [CH_4]_{out}} \times 100\%$$

where m standed for the loading mass of catalyst, ω_{Ni} was the mass fraction of nickel.

3. Results and discussion

3.1. Characterization results

As determined in Table 1 by ICP-OES, Ni loading was 9.3 wt% in Ni/SiO_2 close to the calculative 10 wt%. After coating with ZrO_2, a normal nickel loading was 7.9 wt% and 7.6 wt % for $Ni/SiO_2@2ZrO_2$ and $Ni/SiO_2@4ZrO_2$. To identify the crystallographic structure of

synthesized materials, the power X-ray diffraction study was employed and illustrated in Fig. 1. All catalysts displayed a typical broad peak at 22° that was owing to amorphous silica spheres [45]. The reduced Ni/SiO_2 catalyst showed three shark peaks concentrated upon 44.5°, 52.0° and 76.5°, which were assigned to (111), (200), and (220) plane of cubic metallic Ni phase, respectively, according to JCPDS 04–0850. Whereas the overt decrease in the intensity of Ni peaks was appeared in $Ni/SiO_2@2ZrO_2$ and $Ni/SiO_2@4ZrO_2$, which was due to the coating with ZrO_2. Beyond that $Ni/SiO_2@4ZrO_2$ also exhibited additional diffraction peaks at 30.3°, 35.4°, 50.4° and 59.5°, which were ascribed to tetragonal ZrO_2 crystal phase (JCPDS 96-210-0390). It manifested that ZrO_2 had been successfully prepared. However, $Ni/SiO_2@2ZrO_2$ exhibited no the characteristic peaks of zirconium, probably because less zirconium was uniformly distributed in the catalyst.

The reduction behavior of the calcined Ni/SiO_2, $Ni/SiO_2@2ZrO_2$ and $Ni/SiO_2@4ZrO_2$ was investigated using H_2-TPR experiments, as shown in Fig. 2a. The reduction temperature of NiO species was linked with the interaction strength of Ni species with the support and the higher was the reduction temperature, the greater was the metal-support interaction strength [46,47]. Only one reduction peak was observed for three samples that was linked to the reduction of the whole Ni^{2+} species. The reduction temperature of Ni/SiO_2 was positioned at 383 °C, however that of $Ni/SiO_2@2ZrO_2$ and $Ni/SiO_2@4ZrO_2$ centered at 438 °C and 474 °C, respectively. Therefore, after coating with ZrO_2, there was stronger interaction between surface NiO and support which could stabilize Ni species at high temperature. The amount of H_2 consumption for Ni/SiO_2 was about 1.19 mmol/g_{cat}, which was slightly lower than the theoretical value of 1.20 mmol/g_{cat}. On the contrary, H_2 consumption was approximately 1.38 mmol/g_{cat} for $Ni/SiO_2@4ZrO_2$, which was greater than the theoretical value. This indicated that the lattice oxygen on zirconia surface was removable, whereas that on silica surface could not mobilized.

For the sake of comparing the CO_2 adsorption capacity and accessibility of Ni/SiO_2, $Ni/SiO_2@2ZrO_2$ and $Ni/SiO_2@4ZrO_2$, CO_2-TPD was performed and the results were displayed in Fig. 2b. Typically, according to the desorption temperature, the desorption peak lower than 200 °C was ascribed to CO_2 adsorption on the weak basic sites, and the desorption peak centered at 200–400 °C was attributed to intermediate adsorption basic sites, while the desorption peak higher than 400 °C was due to strongly chemisorbed CO_2 sites [48]. Ni/SiO_2 exhibited the weak (155 °C), intermediate (268 °C) and strong (622 °C) types of CO_2 adsorption sites. However, $Ni/SiO_2@2ZrO_2$ showed simply two peaks, one smaller peak of the representative weak (165 °C) types of CO_2 adsorption sites and another prominent peak (318 °C) of typical intermediate CO_2 adsorption sites. When coating with more ZrO_2, there was only one outstanding adsorption peak centered around 327 °C present to $Ni/SiO_2@4ZrO_2$. It suggested that the introduced ZrO_2 to the catalyst surface could improve the adsorption performance for CO_2 molecules which was attributed to the increase in intermediate adsorption basic sites. As manifested in the literature [49], the Lewis basicity of O^{2-} vacancies on the surface of ZrO_2 may make them alkaline sites for CO_2 adsorption. Hence, detailed comparing Ni/SiO_2 and $Ni/SiO_2@4ZrO_2$, apart from the intermediate adsorption for CO_2 active sites, Ni/SiO_2 also furnished weak and strong adsorption active sites for CO_2 element. But as we know, during the reaction, the weakly adsorbed carbon dioxide could be not broken of the chemical bonds between C-O, and desorption from the active sites became very difficult owing to the strongly adsorbed sites. Therefore, it was not conducive to the CO_2 conversion reaction for extremely weak or fairly strong adsorption of carbon dioxide to the catalyst surface. It was the medium alkaline site that acted an important part in the adsorption and activation of carbon dioxide [50], due to the formation of many intermediates, such as HCO_3^-, b-CO_3^{2-}, m-CO_3^{2-} or carboxylate on this site. In summary, $Ni/SiO_2@4ZrO_2$ showed better carbon dioxide adsorption performance for CO_2 hydrogenation.

The surface chemical state of reduced Ni/SiO_2, $Ni/SiO_2@2ZrO_2$ and $Ni/SiO_2@4ZrO_2$ were showed in the XPS results. In spectra of Ni 2p (Fig. 3a) all samples displayed three fitted peaks, one peak appeared at about 852.6 eV was assigned to Ni^0 and another peak centered at approximately 855.7 eV with a satellite peak signal centered at 861.0 eV was attributed to Ni^{2+} in the NiO phase [51,52]. Further observation revealed that after coating with ZrO_2, the binding energy of Ni^0 and Ni^{2+} over $Ni/SiO_2@2ZrO_2$ and $Ni/SiO_2@4ZrO_2$ both shifted to the higher binding energy by 0.4 and 0.6 eV respectively, indicated a stronger interaction between the Ni species and support. The O 1s XPS spectra was depicted in Fig. 3b. For $Ni/SiO_2@2ZrO_2$ and $Ni/SiO_2@4ZrO_2$, the O 1s XPS spectra were deconvoluted into three main contributions, and the first peak at a high binding energy value of about 532.6 eV was assigned to surface lattice oxygen in SiO_2 (the same as that at 532.4 eV in Ni/SiO_2). The second peak at 531.0 eV was attributed to surface adsorption oxygen (O_β: O^{2-}, O_2^{2-}, or O^-), that was correlated to oxygen vacancy of zirconia [2,53,54]. The peak at the low binding energy of 530.0 eV was ascribed to lattice oxygen (O_α) of ZrO_2 [53]. As shown in Fig. 3c, by back-convolution of Zr 3d spectra, both $Ni/SiO_2@2ZrO_2$ and $Ni/SiO_2@4ZrO_2$ showed the presence of a secondary sub-oxide signal peak at 181.6 eV, which was recorded as $Zr^{\delta+}$, due to a lower oxidation state than that of the lattice Zr^{4+} (binding energy = 182.2 eV). This indicated the presence of interfacial oxygen vacancies [55]. The value of $Zr^{\delta+}/(Zr^{\delta+}+Zr^{4+})$ and $O_\beta/(O_\alpha+O_\beta)$ was 0.24, 0.36 and 0.35, 0.60 respectively in $Ni/SiO_2@2ZrO_2$ and $Ni/SiO_2@4ZrO_2$ by the fitted XPS data. The XPS data (Fig. S1) of the oxidized catalysts also revealed the presence of more Ni^{3+} phases over ZrO_2 coated catalyst that provided the evidence of the formation of more oxygen vacancies, especially evident in $Ni/SiO_2@4ZrO_2$. The fitted results of the XPS spectra were recorded in Table 1. Just so you know, XPS was tested to measure the
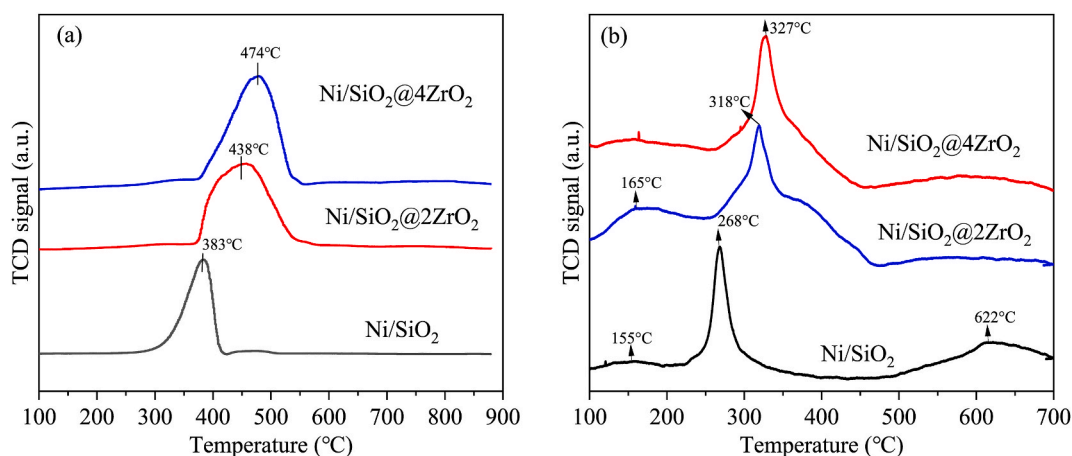
Table 1
Element composition and properties of samples.

Catalysts	Ni loading (wt.%)[a]	Bulk Ni/Zr (molar ratio)[a]	Surface Ni/Zr (molar ratio)[b]	$Zr^{\delta+}/(Zr^{\delta+}+Zr^{4+})$[b]	$O_\beta/(O_\alpha+O_\beta)$[b]
Ni/SiO_2	9.3	–	–	–	–
$Ni/SiO_2@2ZrO_2$	7.9	1.64	0.55	0.24	0.35
$Ni/SiO_2@4ZrO_2$	7.6	1.32	0.20	0.36	0.60

[a] Ni content in the catalysts was analyzed by ICP-OES.
[b] Measured by XPS.
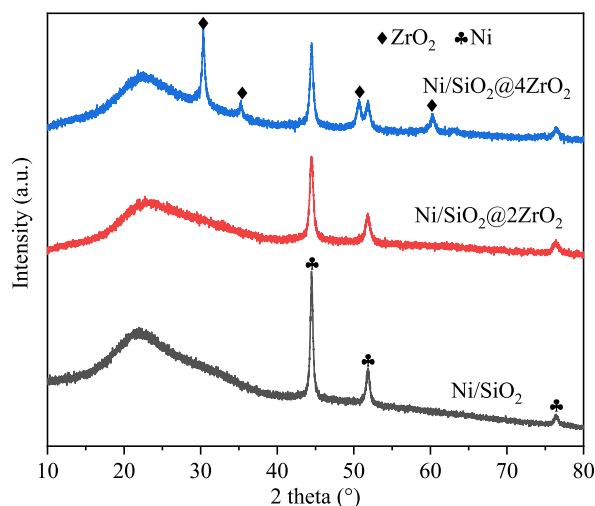
**Fig. 1.** XRD patterns of reduced Ni/SiO_2, $Ni/SiO_2@2ZrO_2$ and $Ni/SiO_2@4ZrO_2$ samples.

Fig. 2. (a) H_2-TPR of calcined Ni/SiO_2, $Ni/SiO_2@2ZrO_2$ and $Ni/SiO_2@4ZrO_2$, (b) CO_2-TPD of reduced Ni/SiO_2, $Ni/SiO_2@2ZrO_2$ and $Ni/SiO_2@4ZrO_2$.

surface composition, whereas ICP-OES was performed to achieve the bulk composition of catalyst. According to XPS results, the surface Ni/Zr mole ratio for $Ni/SiO_2@2ZrO_2$ and $Ni/SiO_2@4ZrO_2$ was 0.55 and 0.20, which was far below the bulk Ni/Zr mole ratio of 1.64 and 1.32 determined by ICP-OES. This showed that the introduced ZrO_2 was mainly coated on the surface of the catalyst.

The morphology and particle dimension of the reduced Ni/SiO_2, $Ni/SiO_2@2ZrO_2$ and $Ni/SiO_2@4ZrO_2$ catalysts were investigated by TEM and the TEM images was displayed in Fig. 4. As shown in the picture, for the three catalysts nickel particles were distributed on the support and exhibited spherical morphology. Apparently, most of the nickel particles were concentrated at 6–9 nm in the reduced Ni/SiO_2 and $Ni/SiO_2@2ZrO_2$ catalyst, whereas that were focused on 6–7 nm in the reduced $Ni/SiO_2@4ZrO_2$ (Fig. 4a-f). This indicated the good thermal stability after calcination and reduction treatment due to the coating with ZrO_2. The reason for the difference in Ni particle size was likely due to the influence of the reduction process. High-temperature reduction technology could inevitably accelerate metal sintering and agglomeration because of the Ostwald ripening. After coating with ZrO_2, the ZrO_2 shell acted as a spatial isolation role that could prevent the aggregation and sintering of nickel particles. Therefore, the average particles size of metal nickel for $Ni/SiO_2@4ZrO_2$ will be smaller than that for Ni/SiO_2. In addition, in the reduced $Ni/SiO_2@4ZrO_2$ (Fig. 4g and h), core-shell structure that consisting of zirconia shell and Ni core was clearly presented. The HRTEM image shown in Fig. 4h further obviously visualized the lattice fringe spacing of 0.20 nm and 0.316 nm in the core-shell location, which were ascribed to the crystal lattice planes of Ni (1 1 1) and ZrO_2 (1 1 1), respectively.

3.2. Catalysis in RWGS

The catalytic activity of Ni/SiO_2, $Ni/SiO_2@2ZrO_2$ and $Ni/SiO_2@4ZrO_2$ for CO_2 hydrogenation to CO were investigated at
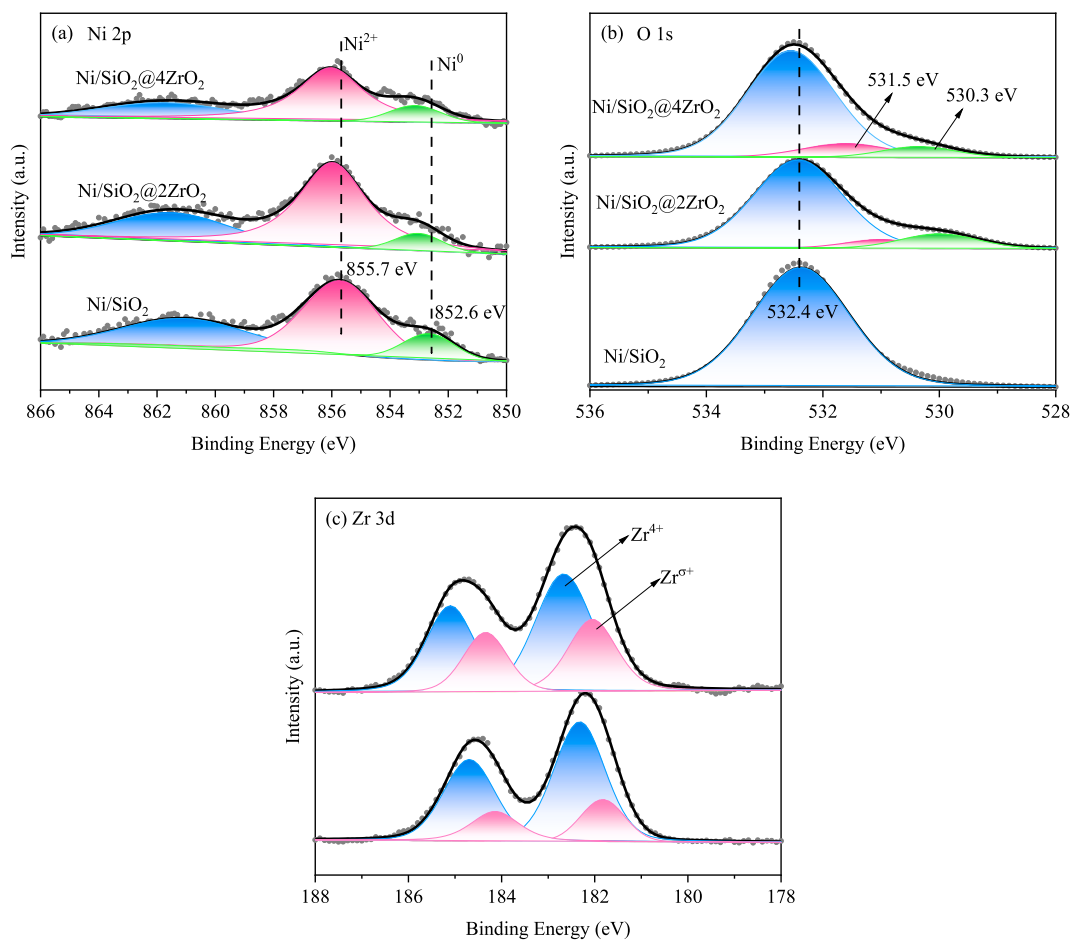
Fig. 3. XPS profiles of (a) Ni 2p, (b) O 1s, (c) Zr 3d in the reduced Ni/SiO$_2$, Ni/SiO$_2$@2ZrO$_2$ and Ni/SiO$_2$@4ZrO$_2$ catalysts.

atmospheric pressure under the weight hourly space velocity (WHSV) of 120000 mL/(g$_{cat}$·h) and 150000 mL/(g$_{cat}$·h). In the CO$_2$ RWGS process, besides hydrogenation product of CO and remained CO$_2$, the only by-product of CH$_4$ was also detected (not listed in the article). The reaction results were shown in Fig. 5. As seen in Fig. 5a, regardless of the catalysts tested, the CO$_2$ conversion was closely related to the reaction temperature and gradually increased from 400 °C to 600 °C, then steadily decreased from 600 °C to 400 °C. This was consistent with the endothermic properties of the RWGS reaction. Further detailed comparison under the GHSV of 120000 mL/ (gcat·h) that when the reaction temperature went from 400 °C to 600 °C, Ni/SiO$_2$ exhibited increased CO$_2$ conversion rates from 1.66 mmol/(g$_{Ni}$·s) to 2.66 mmol/(g$_{Ni}$·s), and that Ni/SiO$_2$@2ZrO$_2$ and Ni/SiO$_2$@4ZrO$_2$ from 1.72 mmol/(g$_{Ni}$·s) to 3.07 mmol/(g$_{Ni}$·s) and from 1.85 mmol/(g$_{Ni}$·s) to 3.17 mmol/(g$_{Ni}$·s), respectively. And it was clear that Ni/SiO$_2$@4ZrO$_2$ showed higher CO$_2$ conversion rates than Ni/SiO$_2$ and Ni/SiO$_2$@2ZrO$_2$. However, when the reaction temperature was down from 600 °C to 400 °C, the CO$_2$ conversion rates of Ni/SiO$_2$ were decreased from 2.66 mmol/(g$_{Ni}$·s) to 1.05 mmol/(g$_{Ni}$·s), that of Ni/SiO$_2$@2ZrO$_2$ and Ni/SiO$_2$@4ZrO$_2$ was decreased from 3.07 mmol/(g$_{Ni}$·s) to 1.33 mmol/(g$_{Ni}$·s) and from 3.17 mmol/(g$_{Ni}$·s) to 1.53 mmol/(g$_{Ni}$·s), respectively. It was obvious that the catalytic activity of Ni/SiO$_2$ decreased substantially. It was also surprising to discover that the activity of all the three catalysts was decreased by comparing the CO$_2$ conversion rate at the reaction temperature of initial 400 °C with the final 400 °C, and the rate of decline was 60.5 %, 56.7 % and 51.7 % for Ni/SiO$_2$, Ni/SiO$_2$@2ZrO$_2$ and Ni/SiO$_2$@4ZrO$_2$, respectively. When the GHSV was 150000 mL/(gcat·h), this phenomenon was more remarkable. As the reaction temperature increased from 400 °C to 600 °C, the CO$_2$ conversion rate of the three catalysts augmented steadily, and the catalytic activity was followed by Ni/SiO$_2$@4ZrO$_2$>Ni/SiO$_2$@2ZrO$_2$>Ni/SiO$_2$. But, with the reaction temperature decreasing from 600 °C to 400 °C, the CO$_2$ conversion rates of Ni/SiO$_2$@2ZrO$_2$ and Ni/SiO$_2$@4ZrO$_2$ was dropped from 2.75 mmol/(g$_{Ni}$·s) to 1.01 mmol/(g$_{Ni}$·s) and from 2.93 mmol/(g$_{Ni}$·s) to 1.49 mmol/(g$_{Ni}$·s), respectively, and that of Ni/SiO$_2$ was decreased from 2.43 mmol/(g$_{Ni}$·s) to 0.50 mmol/(g$_{Ni}$·s). And the rate of decline was 79.2 %, 63.0 % and 48.9 % for Ni/ SiO$_2$, Ni/SiO$_2$@2ZrO$_2$ and Ni/SiO$_2$@4ZrO$_2$. Hence, when coating with ZrO$_2$, the activity stability of the catalyst was enhanced, that was, good resistance to particle aggregation.

The results of CO selectivity under the GHSV of 120000 mL/(g$_{cat}$·h) and 150000 mL/(g$_{cat}$·h) for Ni/SiO$_2$, Ni/SiO$_2$@2ZrO$_2$ and Ni/ SiO$_2$@4ZrO$_2$ were listed in Fig. 5b and d. It was obvious that, despite of the reaction temperature, Ni/SiO$_2$@2ZrO$_2$ and Ni/SiO$_2$@4ZrO$_2$ exhibited a higher CO selectivity, particularly obvious in the low temperature range, compared with Ni/SiO$_2$. This indicated that the
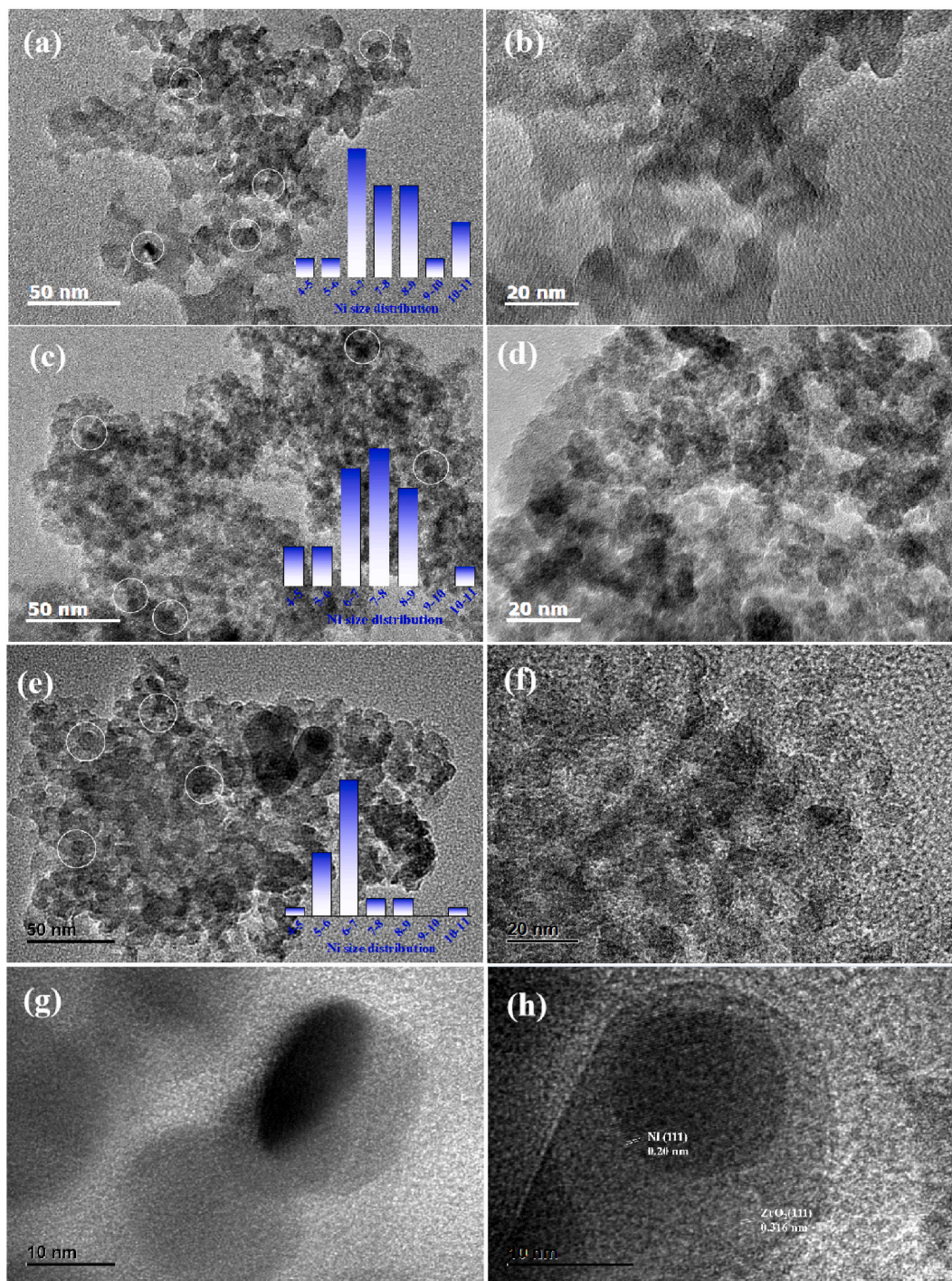
Fig. 4. TEM images of the reduced Ni/SiO$_2$ (a), Ni/SiO$_2$@2ZrO$_2$ (b) and Ni/SiO$_2$@4ZrO$_2$(c, d).

addition of ZrO$_2$ could obviously improve the CO selectivity. And when coating with ZrO$_2$, there was a more steady trend of change for CO selectivity with the variation in temperature, especially for Ni/SiO$_2$@4ZrO$_2$. It was again proved that ZrO$_2$ coated nickel-based catalyst possessed better activity stability. There was an unexpected phenomenon that the CO selectivity was higher at the reaction temperature of the final 400 °C than that of the initial 400 °C. When using GHSV of 120000 mL/(g$_{cat}$·h), the reaction started at 400 °C with selectivity of CO as 57.2 %, 73.9 % and 79.8 %, while finished at 400 °C with selectivity of CO as 64.6 %, 87.8 % and 92.8 % for Ni/SiO$_2$, Ni/SiO$_2$@2ZrO$_2$ and Ni/SiO$_2$@4ZrO$_2$. When using GHSV of 150000 mL/(g$_{cat}$·h), this phenomenon was particularly obvious. The CO selectivity of Ni/SiO$_2$, Ni/SiO$_2$@2ZrO$_2$ and Ni/SiO$_2$@4ZrO$_2$ at the initial 400 °C was 45.6 %, 58.5 % and 63.2 %, and that at the
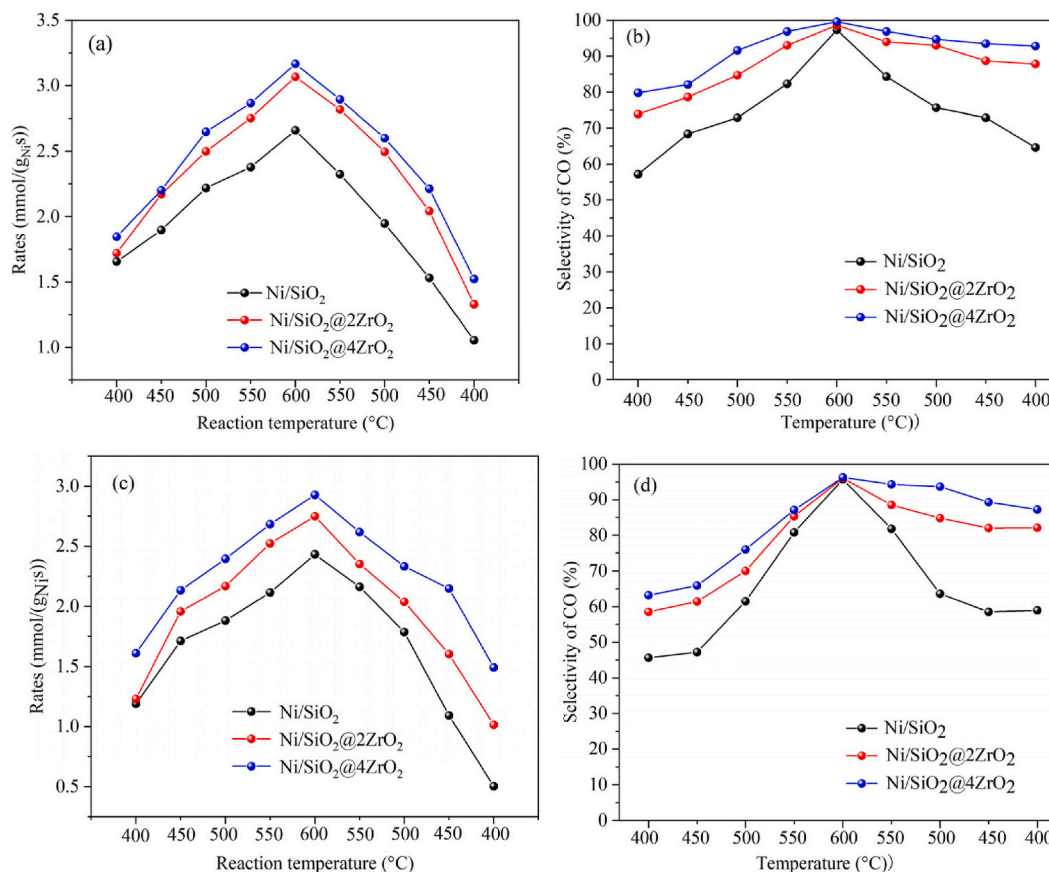
Fig. 5. Catalytic activity of Ni/SiO_2, $Ni/SiO_2@2ZrO_2$ and $Ni/SiO_2@4ZrO_2$ under various reaction temperatures. (a, b) GHSV = 120000mL/(g_{cat}·h), (c, d) GHSV = 150000mL/(g_{cat}·h).

final 400 °C was 58.9 %, 82.1 % and 87.2 %. The increment rate was respectively 29.2 %, 40.3 % and 38.0 %. The similar situation was found in this report and the presence of CO_2/H_2 or CH_4 atmosphere modified the structural and/or surface properties of nickel sites and suppressed further formation of methane [56].

The durability test of Ni/SiO_2, $Ni/SiO_2@2ZrO_2$ and $Ni/SiO_2@4ZrO_2$ at 600 °C under the WHSV of 150000 mL/(g_{cat}·h) was also measured for 72 h during CO_2 RWGS reaction. As shown in Fig. 6a, for Ni/SiO_2, the CO_2 conversion rates were obviously declined from 3.03 mmol/(g_{Ni}.s) to 2.88 mmol/(g_{Ni}.s) after 72 h on stream. While the conversion rates of CO_2 over $Ni/SiO_2@2ZrO_2$ and $Ni/SiO_2@4ZrO_2$ remained almost unchanged as approximately 3.60 mmol/(g_{Ni}.s) and 3.80 mmol/(g_{Ni}.s) at 72 h. The CO selectivity tabulated in Fig. 6b over Ni/SiO_2 and $Ni/SiO_2@2ZrO_2$ was maintained at about 95 % and 96 %, while that over $Ni/SiO_2@4ZrO_2$ was stayed around 100 %. Besides, the XRD (Fig. 6c) of the used $Ni/SiO_2@4ZrO_2$ exhibited the characteristic diffraction peaks of Ni and ZrO_2, with the same peak location and peak intensity to the fresh $Ni/SiO_2@4ZrO_2$. Meanwhile, the TEM images (Fig. 6d) of the used $Ni/SiO_2@4ZrO_2$ showed an excellent dispersion without evident aggregation and particle growth, suggesting a good resistance to metal sintering. This indicated that the coating of ZrO_2 on Ni/SiO_2 surface could achieved high activity and CO selectivity, and effectively improve the activity stability of the nickel-based catalyst.

Therefore the superior CO_2 conversion rate and CO selectivity, as well as stability of the core-shell $Ni/SiO_2@4ZrO_2$ catalyst should be due to the facilitation of zirconia. First of all, $Ni/SiO_2@4ZrO_2$ possessed rich medium-strength CO_2 active sites and abundant oxygen vacancies provided by ZrO_2 that facilitated the activation and reduction of CO_2, while SiO_2 was merely serving as a dispersive carrier with no oxygen vacancies. For CO_2 RWGS reaction, carbon dioxide must be firstly adsorbed efficiently on the catalyst surface (or surface oxygen vacancy) to form activated carbon species, then further reacted with atomic hydrogen to form CO and H_2O. Therefore, it was conducive of effective active sites and oxygen vacancies to the conversion of carbon dioxide. Secondly, ZrO_2 had hydrophilic characteristics that was conducive to the desorption of produced water, and this would definitely facilitate the RWGS reaction. Thirdly, after coating with ZrO_2, there was a enhanced interaction between Ni and support which favored the formation of CO. Fourthly, the ZrO_2 shell acted as a spatial isolation role that could prevent the aggregation and sintering of nickel particles. This could explain the high reaction stability of $Ni/SiO_2@4ZrO_2$.
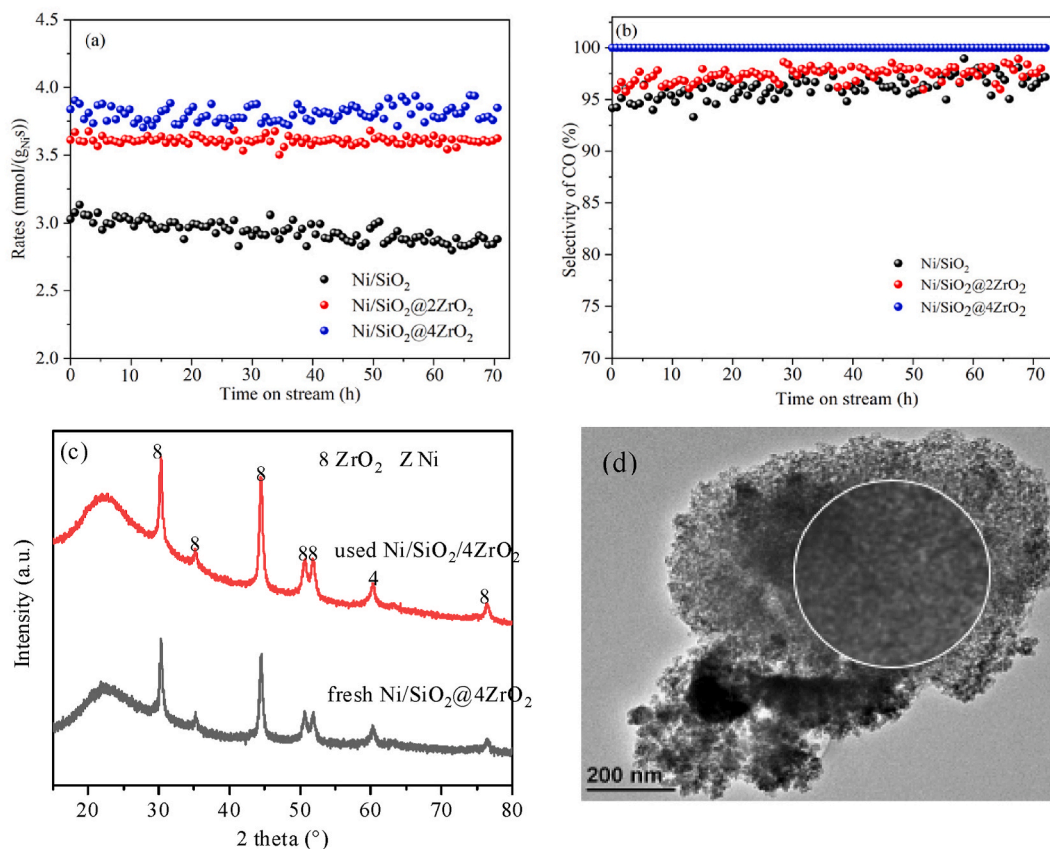
Fig. 6. Durability test of Ni/SiO$_2$, Ni/SiO$_2$@2ZrO$_2$ and Ni/SiO$_2$@4ZrO$_2$ (a, b); XRD pattern (c) and TEM image (d) of the used Ni/SiO$_2$@4ZrO$_2$.

4. Conclusions

This work gave a new perspective for the application of Ni/SiO$_2$@ZrO$_2$ for carbon dioxide hydrogenation reaction. The Ni/SiO$_2$@ZrO$_2$ catalyst was prepared by coating with ZrO$_2$ on the Ni/SiO$_2$ surface via in situ hydrothermal synthesis method. TEM results revealed that the catalyst exhibited a distinct core-shell structure with a ZrO$_2$ shell, as well as uniform particle dispersion. H$_2$-TPR and XPS profiles indicated the evidence of enhanced metal-support interaction and the rich oxygen vacancy in the Ni/SiO$_2$@4ZrO$_2$ catalyst. CO$_2$-TPD studies confirmed Ni/SiO$_2$@4ZrO$_2$ having abundant medium-strength CO$_2$ adsorption sites. These advantages endowed Ni/SiO$_2$@4ZrO$_2$ with superior hydrogenation activity and selectivity to CO as well as stability for the CO$_2$ RWGS reaction. Therefore, the materials with core-shell structure, wherein the shell could protect metal particles from further aggregation and optimize the surface or/and electronic properties of catalyst, was expected to be further developed and utilized.

CRediT authorship contribution statement

Sha Cui: Writing – original draft, Visualization, Methodology, Investigation, Funding acquisition, Formal analysis, Data curation. **Zhe Wang:** Writing – review & editing, Resources, Project administration, Investigation, Funding acquisition. **Honggang Zhao:** Writing – review & editing, Supervision, Resources, Project administration, Investigation, Funding acquisition. **Houxiang Sun:** Visualization, Project administration, Funding acquisition, Data curation. **Qinhong Wei:** Visualization, Validation, Supervision, Resources, Conceptualization. **Luhui Wang:** Visualization, Validation, Supervision, Resources, Conceptualization.

Data availability statement

The authors confirmed that the data supporting the findings of this study were available within the article.

Funding statement

Program (No. 2023NSFSC0096).

Declaration of competing interest

Appendix A. Supplementary data

Supplementary data to this article can be found online at https://doi.org/10.1016/j.heliyon.2024.e40697.

References

[1] M. Siddik, M. Islam, A.K.M.M. Zaman, M.M. Hasan, Current status and correlation of fossil fuels consumption and greenhouse gas emissions, Int. J. Energy Environ. Econ. 28 (2021) 103–119.

[2] K.H. Han, W.S. Yu, L.L. Xu, Z.Y. Deng, H. Yu, F.G. Wang, Reducing carbon deposition and enhancing reaction stability by ceria for methane dry reforming over Ni@SiO$_2$@CeO$_2$ catalyst, Fuel 291 (2021) 120182.

[3] S. Ding, Y. Liu, Adsorption of CO$_2$ from flue gas by novel seaweed-based KOH activated porous biochars, Fuel 260 (2020) 116382.

[4] A.N. Kuhn, R.C. Park, S.Y. Yu, D. Gao, C. Zhang, Y.H. Zhang, H. Yang, Valorization of carbon dioxide into C1 product via reverse water gas shift reaction using oxide-supported molybdenum carbides, Carbon Future 1 (2024) 9200011.

[5] F. Zhang, W. Chen, W. Li, Recent advances in the catalytic conversion of CO$_2$ to chemicals and demonstration projects in China, Mol. Catal. 541 (2023) 113093.

[6] Y.L. Zheng, H.C. Liu, Y.W. Zhang, Engineering heterostructured nanocatalysts for CO$_2$ transformation reactions: advances and perspectives, ChemSusChem 13 (2020) 6090–6123.

[7] G. Centi, E.A. Quadrelli, S. Perathoner, Catalysis for CO$_2$ conversion: a key technology for rapid introduction of renewable energy in the value chain of chemical industries, Energy Environ. Sci. 6 (2013) 1711–1731.

[8] I. Sreedhar, Y. Varun, S.A. Singh, A. Venugopal, B.M. Reddy, Developmental trends in CO$_2$ methanation using various catalysts, Catal. Sci. Technol. 9 (2019) 4478–4504.

[9] X. Yang, X. Su, X. Chen, H. Duan, B. Liang, Q. Liu, X. Liu, Y. Ren, Y. Huang, T. Zhang, Promotion effects of potassium on the activity and selectivity of Pt/zeolite catalysts for reverse water gas shift reaction, Appl. Catal., B 216 (2017) 95–105.

[10] H.S. Dong, M.N. Jung, Y.P. Zhang, S. Wang, S.P. Ding, Supported noble metal-based catalysts for thermal CO$_2$ hydrogenation to CO, Mol. Catal. 560 (2024) 114133.

[11] A.I.M. Rabee, D. Zhao, S. Cisneros, C.R. Kreyenschulte, V. Kondratenko, C. Bartling, C. Kubis, E.V. Kondratenko, A. Bruckner, J. Rabeah, Role of interfacial oxygen vacancies in low-loaded Au-based catalysts for the low-temperature reverse water gas shift reaction, Appl. Catal., B 321 (2023) 122083.

[12] S. Li, Y. Xu, Y. Chen, W. Li, L. Lin, M. Li, Y. Deng, X. Wang, B. Ge, C. Yang, S. Yao, J. Xie, Y. Li, X. Liu, D. Ma, Tuning the selectivity of catalytic carbon dioxide hydrogenation over iridium/cerium oxide catalysts with a strong metal-support interaction, Angew. Chem. Int. Ed. 56 (2017) 10761–10765.

[13] Y. Choi, G.D. Sim, U. Jung, Y. Park, M.H. Youn, D.H. Chun, G.B. Rhim, K.Y. Kim, K.Y. Koo, Copper catalysts for CO$_2$ hydrogenation to CO through reverse water–gas shift reaction for e-fuel production: fundamentals, recent advances, and prospects, Chem. Eng. J. 492 (2024) 152283.

[14] B. Lu, K. Kawamoto, Transition metal-rich mesoporous silicas and their enhanced catalytic properties, Catal. Sci. Technol. 4 (2014) 4313–4321.

[15] F.M. Sun, C.F. Yan, Z.D. Wang, C.Q. Guo, S.L. Huang, Ni/Ce–Zr–O catalyst for high CO$_2$ conversion during reverse water gas shift reaction (RWGS), Int. J. Hydrogen Energy 40 (2015) 15985–15993.

[16] C. Voigt, R.E. Lamprecht, M.E. Marushchak, S.E. Lind, A. Novakovskiy, M. Aurela, P.J. Martikainen, C. Biasi, Warming of subarctic tundra increases emissions of all three important greenhouse gases–carbon dioxide, methane, and nitrous oxide, Global Change Biol. 23 (2017) 3121–3138.

[17] M.C. Alvarez-Galvan, N. Mota, M. Ojeda, S. Rojas, R.M. Navarro, J.L.G. Fierro, Direct methane conversion routes to chemicals and fuels, Catal. Today 171 (2011) 15–23.

[18] H.C. Wu, Y.C. Chang, J.H. Wu, J.H. Lin, I.K. Lin, C.S. Chen, Methanation of CO$_2$ and reverse water gas shift reactions on Ni/SiO$_2$ catalysts: the influence of particle size on selectivity and reaction pathway, Catal. Sci. Technol. 5 (2015) 4154–4163.

[19] R.V. Gonçalves, L.L.R. Vono, R. Wojcieszak, C.S.B. Dias, H. Wender, E. Teixeira-Neto, L.M. Rossi, Selective hydrogenation of CO$_2$ into CO on a highly dispersed nickel catalyst obtained by magnetron sputtering deposition: a step towards liquid fuels, Appl. Catal. B Environ. 209 (2017) 240–246.

[20] C. Zhang, R.Y. Zhang, Y.X. Liu, X.X. Wu, H. Wang, Q.F. Ge, X.L. Zhu, Blocking methanation during reverse water gas shift reaction on Ni/SiO$_2$ catalysts by surface Ag, ChemCatChem 15 (2023) e202201284.

[21] L. Yang, L. Pastor-Pérez, S. Gu, A. Sepúlveda-Escribano, T.R. Reina, Highly efficient Ni/CeO$_2$-Al$_2$O$_3$ catalysts for CO$_2$ upgrading via reverse water-gas shift: effect of selected transition metal promoters, Appl. Catal. B Environ. (2018) 464–471.

[22] B. Rutherford, C. Panaritis, E. Pahija, C. Martin, B. Patarachao, J. Shadbahr, F. Bensebaa, G.S. Patience, D.C. Boffito, Ni nanoparticles on Co$_3$O$_4$ catalyze the reverse water–gas shift with 95% CO selectivity at 300 °C, Fuel 348 (2023) 128523.

[23] W.X. Wang, X.K. Li, Y. Zhang, R. Zhang, H. Ge, J.C. Bi, M.X. Tang, Strong metal-support interactions between Ni and ZnO particles and their effect on the methanation performance of Ni/ZnO, Catal. Sci. Technol. 7 (2017) 4413–4421.

[24] L.H. Wang, S.X. Zhang, Y. Liu, Reverse water gas shift reaction over Co-precipitated Ni-CeO$_2$ catalysts, J. Rare Earths 26 (2008) 66–70.

[25] F. Rahmani, M. Haghighi, P. Estifaee, Synthesis and characterization of Pt/Al$_2$O$_3$–CeO$_2$ nanocatalyst used for toluene abatement from waste gas streams at low temperature: conventional vs. plasma–ultrasound hybrid synthesis methods, Microporous Mesoporous Mater. 185 (2014) 213–223.

[26] M.T. Rodrigues, P.C. Zonetti, O.C. Alves, E.F. Sousa-Aguiar, L.E.P. Borges, L.G. Appel, RWGS reaction employing Ni/Mg(Al,Ni)O-The role of the O vacancies, Appl. Catal., A 543 (2017) 98–103.

[27] H.C. Wu, Y.C. Chang, J.H. Wu, J.H. Lin, I.K. Lin, C.S. Chen, Methanation of CO$_2$ and reverse water gas shift reactions on Ni/SiO$_2$ Catalysts: the influence of particle size on selectivity and reaction pathway, Catal. Sci. Technol. 5 (2015) 4154–4163.

[28] N. Liu, S. Cui, Z.Y. Jin, Z. Cao, H. Liu, S.Q. Yang, X.M. Zheng, L.H. Wang, Highly dispersed and stable Ni/SiO$_2$ catalysts prepared by urea-assisted impregnation method for reverse water–gas shift reaction, Processes 11 (2023) 1353.

[29] E. Gioria, P. Ingale, F. Pohl, R. Naumann d'Alnoncourt, A. Thomas, F. Rosowski, Boosting the performance of Ni/Al$_2$O$_3$ for the reverse water gas shift reaction through formation of CuNi nanoalloys, Catal. Sci. Technol. 12 (2022) 474–487.

[30] L.D. Deng, X. Ai, F.Q. Xie, G.L. Zhou, Efficient Ni-based catalysts for low-temperature reverse water-gas shift (RWGS) reaction, Chem. Asian J. 16 (2021) 949–958.

[31] J. Gandara-Loe, Q. Zhang, J. José VilloraPicó, A. Sepulveda-Escribano, L. Pastor-Pérez, T.R. Reina, Design of full-temperature-range RWGS catalysts: impact of alkali promoters on Ni/CeO$_2$, Energy Fuels 36 (2022) 6362–6373.

[32] R. Zhou, N. Rui, Z. Fan, C. Liu, Effect of the structure of Ni/TiO$_2$ catalyst on CO$_2$ methanation, Int. J. Hydrogen Energy 41 (2016) 22017–22025.

[33] G. Torres-Sempere, J. González-Arias, A. Penkova, J.L. Santos-Muñoz, L.F. Bobadilla, J.A. Odriozola, L. Pastor-Pérez, T.R. Reina, CO$_2$ Conversion via low-temperature RWGS enabled by multicomponent catalysts: could transition metals outperform Pt? Top. Catal. (2024) 1–12.

[34] S. Sokolov, J. Radnik, M. Schneider, U. Rodemerck, Low-temperature CO$_2$ reforming of methane over Ni supported on ZnAl mixed metal oxides, Int. J. Hydrogen Energy 42 (2017) 9831–9839.

[35] P.C. Zonetti, S. Letichevsky, A.B. Gaspar, E.F. Sousa-Aguiar, L.G. Appel, The Ni$_x$Ce$_{0.75}$Zr$_{0.25-x}$O$_2$ solid solution and the RWGS, Appl. Catal., A 475 (2014) 48–54.

[36] L.X. Ma, R.P. Ye, Y.Y. Huang, T.R. Reina, X.Y. Wang, C.M. Li, X.L. Zhang, M.H. Fan, R.G. Zhang, J. Liu, Enhanced low-temperature CO$_2$ methanation performance of Ni/ZrO$_2$ catalysts via a phase engineering strategy, Chem. Eng. J. 446 (2022) 137031.

[37] M. Zhang, J.F. Zhang, Y.Q. Wu, Q.D. Pan J.X. ● Zhang, Y.S. Tan, Y.Z. Han, Insight into the effects of the oxygen species over Ni/ZrO$_2$ catalyst surface on methane reforming with carbon dioxide, Appl. Catal. B Environ. 244 (2019) 427–437.

[38] D. Zhang, H.T. Cai, Y.Z. Su, W. Sun, D.R. Yang, G.A. Ozin, Silica samurai: aristocrat of energy and environmental catalysis, Chem Catal. 2 (2022) 1893–1918.

[39] Y. Lou, M. Steib, Q. Zhang, K. Tiefenbacher, A. Horváth, A. Jentys, Y. Liu, J.A. Lercher, Design of stable Ni/ZrO$_2$ catalysts for dry reforming of methane, J. Catal. 356 (2017) 147–156.

[40] P. Gao, F. Li, H.J. Zhan, N. Zhao, F.K. Xiao, W. Wei, L.S. Zhong, H. Wang, Y.H. Sun, Influence of Zr on the performance of Cu/Zn/Al/Zr catalysts via hydrotalcite-like precursors for CO$_2$ hydrogenation to methanol, J. Catal. 298 (2013) 51–60.

[41] X.M. Guo, D.S. Mao, G.Z. Lu, S. Wang, G.S. Wu, Glycine nitrate combustion synthesis of CuO-ZnO-ZrO$_2$ catalysts for methanol synthesis from CO$_2$ hydrogenation, J. Catal. 271 (2010) 178–185.

[42] Z.Y. Lim, C. Wu, W.G. Wang, K.L. Choy, H.F. Yin, Porosity effect on ZrO$_2$ hollow shells and hydrothermal stability for catalytic steam reforming of methane, J. Mater. Chem. A 4 (2016) 153–159.

[43] S. Das, J. Pérez-Ramírez, J.L. Gong, N. Dewangan, K. Hidajat, B.C. ● Kawi S. Gates, Core–shell structured catalysts for thermocatalytic, photocatalytic, and electrocatalytic conversion of CO$_2$, Chem. Soc. Rev. 49 (2020) 2937–3004.

[44] C.T. Wang, E. Guan, L. Wang, X.F. Chu, Z.Y. Wu, J. Zhang, Z.Y. Yang, Y.W. Jiang, L. Zhang, X.J. Meng, B.C. Gates, F.S. Xiao, Product selectivity controlled by nanoporous environments in zeolite crystals enveloping rhodium nanoparticle catalysts for CO$_2$ hydrogenation, J. Am. Chem. Soc. 141 (2019) 8482–8488.

[45] R.S. Dubey, Y. Rajesh, M.A. More, Synthesis and characterization of SiO$_2$ nanoparticles via sol-gel method for industrial applications, Mater. Today: Proc. 2 (2015) 3575–3579.

[46] Y.Z. Wang, R.F. Wu, Y.X. Zhao, Effect of ZrO$_2$ promoter on structure and catalytic activity of the Ni/SiO$_2$ catalyst for CO methanation in hydrogen-rich gases, Catal. Today 158 (2010) 470–474.

[47] W.X. Wang, X.K. Li, Y. Zhang, R. Zhang, H. Ge, J.C. Bi, M.X. Tang, Strong metal–support interactions between Ni and ZnO particles and their effect on the methanation performance of Ni/ZnO, Catal. Sci. Technol. 7 (2017) 4413–4421.

[48] Q. Li, Q.J. Tang, P.Y. Xiong, D.Z. Chen, J.M. Chen, Z.B. Wu, H.Q. Wang, Effect of palladium chemical states on CO$_2$ photocatalytic reduction over g-C$_3$N$_4$: distinct role of single-atomic state in boosting CH$_4$ production, Chin. J. Catal. 46 (2023) 177–190.

[49] W.Z. Li, Z.K. Zhao, Hierarchically structured tetragonal zirconia as a promising support for robust Ni based catalysts for dry reforming of methane, RSC Adv. 6 (2016) 72942–72951.

[50] Y. Zhang, S.J. Park, Au–pd bimetallic alloy nanoparticle-decorated BiPO$_4$ nanorods for enhanced photocatalytic oxidation of trichloroethylene, J. Catal. 355 (2017) 1–10.

[51] J.H. Lin, C.P. Ma, Q. Wang, Y.F. Xu, G.Y. Ma, J. Wang, H.T. Wang, C.L. Dong, C.H. Zhang, M.Y. Ding, Enhanced low-temperature performance of CO$_2$ methanation over mesoporous Ni/Al$_2$O$_3$-ZrO$_2$ catalysts, Appl. Catal. B Environ. 243 (2019) 262–272.

[52] B. Jin, S. Li, Y. Liu, et al., Engineering metal-oxide interface by depositing ZrO$_2$ overcoating on Ni/Al$_2$O$_3$ for dry reforming of methane, Chem. Eng. J. 436 (2022) 135195.

[53] H.L. Wang, Q. Li, J. Chen, J. Chen, H.P. Jia, Efficient solar-driven CO$_2$ methanation and hydrogen storage over nickel catalyst derived from metal–organic frameworks with rich oxygen vacancies, Adv. Sci. 10 (2023) 2304406.

[54] Y.D. Zhou, L. Liu, G.Y. Li, C.W. Hu, Insights into the influence of ZrO$_2$ crystal structures on methyl laurate hydrogenation over Co/ZrO$_2$ catalysts, ACS Catal. 11 (2021) 7099–7113.

[55] Y.Z. Ge, T.S. Zou, A.J. Martín, T. Block, R. Pottgen, J. Pérez-Ramírez, Defective zirconia promotes monometallic iron catalysts for higher alcohol synthesis, Chem Catal. 4 (2024) 101010.

[56] T.S. Galhardo, A.H. Braga, B.H. Arpini, J. Szanyi, R.V. Goncalves, B.F. Zornio, C.R. Miranda, L.M. Rossi, Optimizing active sites for high CO selectivity during CO$_2$ hydrogenation over supported nickel catalysts, J. Am. Chem. Soc. 143 (2021) 4268–4280.